Manuscript submitted to CMES

Local Moving Least Square - One-Dimensional IRBFN Technique: Part I - Natural Convection Flows in Concentric and Eccentric Annuli

D. Ngo-Cong[1,2], N. Mai-Duy[1], W. Karunasena[2] and T. Tran-Cong[1,3]

Abstract: In this paper, natural convection flows in concentric and eccentric annuli are studied using a new numerical method, namely local moving least square - one dimensional integrated radial basis function networks (LMLS-1D-IRBFN). The partition of unity method is used to incorporate the moving least square (MLS) and one dimensional-integrated radial basis function (1D-IRBFN) techniques in an approach that leads to sparse system matrices and offers a high level of accuracy as in the case of 1D-IRBFN method. The present method possesses a Kronecker-Delta function property which helps impose the essential boundary condition in an exact manner. The method is first verified by the solution of the two-dimensional Poisson equation in a square domain with a circular hole, then applied to natural convection flow problems. Numerical results obtained are in good agreement with the exact solution and other published results in the literature.

Keywords: Natural convection, concentric annulus, eccentric annulus, integrated radial basis functions, moving least square, partition of unity; Cartesian grids.

1 Introduction

Natural convection has been investigated both experimentally and numerically by many researchers for its wide applications, including nuclear reactor designs, solar energy systems, cooling of electronic equipments and thermal storage systems. Banerjee, Mukhopadhyay, Sen, and Ganguly (2008) conducted a study of heat transfer in a square enclosure with two discrete heat sources mounted on its bottom wall using finite volume method (FVM). Their work is useful in the design of

[1] Computational Engineering and Science Research Centre, Faculty of Engineering and Surveying, The University of Southern Queensland, Toowoomba, QLD 4350, Australia.
[2] Centre of Excellence in Engineered Fibre Composites, Faculty of Engineering and Surveying, The University of Southern Queensland, Toowoomba, QLD 4350, Australia.
[3] Corresponding author, Email: trancong@usq.edu.au.

efficient heat-removal systems in electronics and MEMS applications. Jubran, Al-Abdali, Al-Hiddabi, Al-Hinai, and Zurigat (2004) simulated convective layers on solar pond walls using three-dimensional FVM for solving conservation equations for mass, chemical species, momentum and energy. They investigated the effects of wall tilt angle and salt concentration on the characteristics of the convective layers. Costa and Raimundo (2010) numerically studied a mixed convection in a heated square enclosure with a rotating cylinder within it. They observed that the size of the inner cylinder strongly affects the resulting flow and heat transfer process. Their simulation can be used to model real situations where a rotating shaft is used to control the performance of natural convection in an enclosure.

Kuehn and Goldstein (1976) conducted experimental and theoretical studies to investigate the natural convection within an annulus between horizontal concentric cylinders. Their experimental results showed that the flow is steady for small Rayleigh numbers. Their numerical results were in good agreement with their experimental data. Moukalled and Acharya (1996) studied the natural convection in a annulus between concentric horizontal circular and square cylinders using a control volume-based method. Shu and Zhu (2002) employed the differential quadrature (DQ) method to simulate the natural convection in a concentric annulus between a cold outer square cylinder and a heated inner circular cylinder. The DQ method can yield very accurate numerical results owing to its global approximation. However, the irregular physical domain must be transformed into a regular computational domain, and the governing equations as well as the boundary conditions are also transformed into relevant forms in the computational space. Šarler and Perko (2004) presented a radial basis function collocation method for solving natural convection problems in porous media in terms of primitive variables. Recently, Kim, Lee, Ha, and Yoon (2008) employed an immersed boundary method (IBM) based on FVM with non-uniform Cartesian grid distribution for the simulation of natural convection between an inner circular cylinder and an outer square enclosure.

When dealing with incompressible viscous flows in multiply-connected domains using stream function-vorticity formulation, the stream function value on the inner boundaries are unknown and can be determined through a single-valued pressure condition [Lewis (1979)]. Tezduyar, Glowinski, and Liou (1988) proposed a streamline-upwind/Petrov-Galerkin finite element procedure for a computation of two-dimensional fluid flow involving multiply-connected domains based on the vorticity-stream function formulation. The stream function values at the internal boundaries were determined through additional equations obtained by integrating the equation of motion along those boundaries. Shu, Xue, and Zhu (2001) applied the DQ method to the natural convective transfer in an eccentric annulus between a circular inner cylinder and a square outer cylinder. In their work, an explicit for-

mulation of the stream function value on the inner cylinder wall was derived from the single-valued pressure condition.

In the past decades, meshfree methods have become a very interesting research topic as they might have certain advantages over conventional element-based methods. Some of their appealing properties are (i) a significant reduction in discretisation complexity and (ii) suitability for solving problems with moving boundaries and complicated geometry. However, global meshfree methods are not suitable for simulating large-scale problems because they produce very dense system matrices, which leads to the ill-conditioning problem, large storage requirement and a long computational time [Kansa (1990); Zerroukat, Djidjeli, and Charafi (2000); Šarler and Perko (2004)]. In order to overcome this disadvantage, local meshfree methods have been proposed. Shu, Ding, and Yeo (2003) presented a local RBF-based differential quadrature method (local RBF-DQ) for a simulation of natural convection in a square cavity. In their study, three layers of orthogonal grid near and including the boundary were generated for the purpose of imposing the Neumann condition for temperature and vorticity on the wall. The derivatives of the field variables in the boundary conditions were then discretised by the conventional one-sided second order finite difference scheme. Ding, Shu, Yeo, and Lu (2005) employed the local RBF-DQ method for simulation of natural convection in a horizontal eccentric annulus. In their work, the effects of eccentricity and angular position on the flow and thermal fields for medium aspect ratios were studied. The local RBF-DQ method was also used for solving incompressible flow problems including the driven-cavity flow, flow past one isolated cylinder and flow around two staggered circular cylinders [Shu, Ding, and Yeo (2005)]. Šarler and Vertnik (2006) proposed an explicit local radial basis function collocation method for diffusion problems. The method appeared efficient, because it does not deal with a large system of equations like the original Kansa method [Kansa (1990)]. The method was then extended to solve many other problems such as convection-diffusion problems with phase change [Vertnik and Šarler (2006)], a solution of conjugate heat transfer [Divo and Kassab (2007)], and a solution of incompressible turbulent flow [Vertnik and Šarler (2009)]. Recently, Yao, Šarler, and Chen (2011) presented a comparison of three explicit local meshless methods including a local method of approximate particular solutions (LMAPS), a local direct radial basis function collocation method (LDRBFCM), and a local indirect radial basis function collocation method (LIRBFNCM). Three methods were applied to a simple diffusion equation with Dirichlet jump boundary condition based on both uniform and non-uniform node distributions. Their numerical results showed that all methods have high accuracy and improvement of the accuracies with increasing node density and decreasing time step. For random node arrangement, the LMAPS

and the LDRBFCM are more stable than the LIDRBFCM. Some other meshfree methods based on local approximations include meshless local Petrov Galerkin method (MLPG) [Atluri and Zhu (1998)], a point interpolation meshless method based on combining radial and polynomial basis function by Wang and Liu (2002), local multiquadric (LMQ) and local inverse multiquadric (LIMQ) approximation methods by Lee, Liu, and Fan (2003), a moving IRBFN-based Galerkin meshless method proposed by Le, Rabczuk, Mai-Duy, and Tran-Cong (2010).

A different approach for solving PDEs is the so-called Cartesian grid method where the governing equations are discretised by a Cartesian grid which does not conform to the immersed boundaries. This significantly reduces the grid generation cost and has a great potential over the conventional body-fitted methods when solving problems with moving boundaries and complicated geometry. Ye, Mittal, Udaykumar, and Shyy (1999) developed a finite-volume based Cartesian grid method for simulating two-dimensional unsteady, viscous, incompressible flows with complex immersed boundaries. In their method, the immersed boundary is represented by a series of piecewise linear segments. Based on these segments, the control volume near the immersed boundary is reformed into a body-fitted trapezoidal shape. Russell and Wang (2003) presented a Cartesian grid method for solving 2D incompressible viscous flows around multiple moving objects based on stream function-vorticity formulation.

As an alternative to the conventional differentiated radial basis function network (DRBFN) method [Kansa (1990)], Mai-Duy and Tran-Cong (2001a) proposed the use of integration to construct the RBFN expressions (the IRBFN method) for the approximation of a function and its derivatives and for the solution of PDEs. The numerical results showed that the IRBFN method achieves superior accuracy [Mai-Duy and Tran-Cong (2001a); Mai-Duy and Tran-Cong (2001b)]. A one-dimensional integrated radial basis function network (1D-IRBFN) collocation method for the solution of second- and fourth-order PDEs was presented by Mai-Duy and Tanner (2007). Along grid lines, 1D-IRBFN are constructed to satisfy the governing differential equations with boundary conditions in an exact manner. In the 1D-IRBFN method, the Cartesian grids were used to discretise both rectangular and non-rectangular problem domains. The 1D-IRBFN method is much more efficient than the original IRBFN method reported in Mai-Duy and Tran-Cong (2001a). Le-Cao, Mai-Duy, Tran, and Tran-Cong (2011) employed the 1D-IRBFN method to simulate unsymmetrical flows of a Newtonian fluid in multiply-connected domains using the stream-function and temperature formulation. Ngo-Cong, Mai-Duy, Karunasena, and Tran-Cong (2011) extended this method to investigate free vibration of composite laminated plates based on first-order shear deformation theory. Ngo-Cong, Mai-Duy, Karunasena, and Tran-Cong (2012) proposed

a local moving least square - one dimensional integrated radial basis function network method (LMLS-1D-IRBFN) for simulating 2-D steady incompressible viscous flows in terms of stream function and vorticity. The method is based on the partition of unity framework to incorporate the moving least square and 1D-IRBFN techniques in an approach that produces a very sparse system matrix and offers as a high level of accuracy as that of the 1D-IRBFN. Moreover, LMLS-1D-IRBFN shape function possesses the Kronecker-δ property which helps impose the essential boundary condition in an exact manner. In this article, the LMLS-1D-IRBFN is applied to the solution of the stream-function, vorticity and temperature formulation of the natural convection in concentric and eccentric annuli. For the concentric case, the stream function values at the inner and outer boundaries are taken to be zero. For the eccentric case, the stream function value at the outer boundary is taken to be zero, while the stream function at the inner cylinder is unknown and calculated based on the single-valued pressure condition.

The paper is organised as follows. Section 2 describes the notations. The LMLS-1D-IRBFN method is presented in Section 3. The governing equations for natural convection flows are given in Section 4. Several numerical examples are investigated using the proposed method in Section 5. Section 6 concludes the paper.

2 Notations

In the remainder of the article, we use

- the notation $\overline{[\,]}$ for a vector/matrix $[\,]$ that is associated with a segment of a grid line;
- the notation $\widehat{[\,]}$ for a vector/matrix $[\,]$ that is associated with a grid line;
- the notation $\widetilde{[\,]}$ for a vector/matrix $[\,]$ that is associated with the whole set of grid lines;
- the notation $[\,]_{(\eta,\theta)}$ to denote selected rows η and columns θ of the matrix $[\,]$;
- the notation $[\,]_{(\eta)}$ to denote selected components η of the vector $[\,]$;
- the notation $[\,]_{(:,\theta)}$ to denote all rows and selected columns θ of the matrix $[\,]$; and
- the notation $[\,]_{(\eta,:)}$ to denote all columns and selected rows η of the matrix $[\,]$.

3 Local moving least square - one dimensional integrated radial basis function networks technique

A schematic outline of the LMLS-1D-IRBFN method is depicted in Fig. 1. The proposed method with 3-node support domains ($n = 3$) and 5-node local 1D-IRBF networks ($n_s = 5$) is presented here. On an x-grid line $[l]$, a global interpolant for the field variable at a grid point x_i is sought in the form

$$u(x_i) = \sum_{j=1}^{n} \bar{\phi}_j(x_i) u^{[j]}(x_i), \tag{1}$$

where $\left\{\bar{\phi}_j\right\}_{j=1}^{n}$ is a set of the partition of unity functions constructed using MLS approximants [Liu (2003)]; $u^{[j]}(x_i)$ the nodal function value obtained from a local interpolant represented by a 1D-IRBF network $[j]$; n the number of nodes in the support domain of x_i. In (1), MLS approximants are presently based on linear polynomials, which are defined in terms of 1 and x. It is noted that the MLS shape functions possess a so-called partition of unity properties as follows.

$$\sum_{j=1}^{n} \bar{\phi}_j(x) = 1. \tag{2}$$

Relevant derivatives of u at x_i can be obtained by differentiating (1)

$$\frac{\partial u(x_i)}{\partial x} = \sum_{j=1}^{n} \left(\frac{\partial \bar{\phi}_j(x_i)}{\partial x} u^{[j]}(x_i) + \bar{\phi}_j(x_i) \frac{\partial u^{[j]}(x_i)}{\partial x} \right), \tag{3}$$

$$\frac{\partial^2 u(x_i)}{\partial x^2} = \sum_{j=1}^{n} \left(\frac{\partial^2 \bar{\phi}_j(x_i)}{\partial x^2} u^{[j]}(x_i) + 2\frac{\partial \bar{\phi}_j(x_i)}{\partial x} \frac{\partial u^{[j]}(x_i)}{\partial x} + \bar{\phi}_j(x_i) \frac{\partial^2 u^{[j]}(x_i)}{\partial x^2} \right), \tag{4}$$

where the values $u^{[j]}(x_i), \partial u^{[j]}(x_i)/\partial x$ and $\partial^2 u^{[j]}(x_i)/\partial x^2$ are calculated from 1D-IRBFN networks with n_s nodes.

3.1 One-dimensional IRBFN

Consider a segment $[j]$ with n_s nodes on an x-grid line $[l]$ as shown in Fig. 1. The variation of the nodal function $u^{[j]}$ along this segment is sought in the IRBF form. The second-order derivative of $u^{[j]}$ is decomposed into RBFs; the RBF network is then integrated once and twice to obtain the expressions for the first-order derivative

of $u^{[j]}$ and the function $u^{[j]}$ itself as follows.

$$\frac{\partial^2 u^{[j]}(x)}{\partial x^2} = \sum_{k=1}^{n_s} w^{(k)} G^{(k)}(x) = \sum_{k=1}^{n_s} w^{(k)} H_{[2]}^{(k)}(x), \tag{5}$$

$$\frac{\partial u^{[j]}(x)}{\partial x} = \sum_{k=1}^{n_s} w^{(k)} H_{[1]}^{(k)}(x) + c_1, \tag{6}$$

$$u^{[j]}(x) = \sum_{k=1}^{n_s} w^{(k)} H_{[0]}^{(k)}(x) + c_1 x + c_2, \tag{7}$$

where $\left\{w^{(k)}\right\}_{k=1}^{n_s}$ are RBF weights to be determined; $\left\{G^{(k)}(x)\right\}_{k=1}^{n_s} = \left\{H_{[2]}^{(k)}(x)\right\}_{k=1}^{n_s}$ known RBFs; $H_{[1]}^{(k)}(x) = \int H_{[2]}^{(k)}(x)dx$; $H_{[0]}^{(k)}(x) = \int H_{[1]}^{(k)}(x)dx$; and c_1 and c_2 integration constants which are also unknown. An example of RBF, used in this work, is the multiquadrics $G^{(k)}(x) = \sqrt{(x-x^{(k)})^2 + a^{(k)2}}$, $a^{(k)}$ - the RBF width determined as $a^{(k)} = \beta d^{(k)}$, β a positive factor, and $d^{(k)}$ the distance from the k^{th} center to its nearest neighbour.

It is more convenient to work in the physical space than in the network-weight space. The RBF coefficients including two integration constants can be transformed into the physically meaningful nodal variable values through the following relation

$$\vec{u}^{[j]} = \bar{\mathbf{H}} \begin{pmatrix} \bar{w} \\ \bar{c} \end{pmatrix}, \tag{8}$$

where $\bar{\mathbf{H}}$ is an $n_s \times (n_s + 2)$ matrix and given by

$$\mathbf{H} = \begin{bmatrix} H_{[0]}^{(1)}(x_1) & H_{[0]}^{(2)}(x_1) & \ldots & H_{[0]}^{(n_s)}(x_1) & x_1 & 1 \\ H_{[0]}^{(1)}(x_2) & H_{[0]}^{(2)}(x_2) & \ldots & H_{[0]}^{(n_s)}(x_2) & x_2 & 1 \\ \ldots & \ldots & \ldots & \ldots & \ldots & \ldots \\ H_{[0]}^{(1)}(x_{n_s}) & H_{[0]}^{(2)}(x_{n_s}) & \ldots & H_{[0]}^{(n_s)}(x_{n_s}) & x_{n_s} & 1 \end{bmatrix}; \tag{9}$$

$\vec{u}^{[j]} = (u^{(1)}, u^{(2)}, ..., u^{(n_s)})^T$; $\bar{w} = (w^{(1)}, w^{(2)}, ..., w^{(n_s)})^T$ and $\bar{c} = (c_1, c_2)^T$. There are two possible transformation cases.

For a segment $[j]$ *with only interior points:* The direct use of (8) leads to an underdetermined system of equations

$$\vec{u}^{[j]} = \bar{\mathbf{H}} \begin{pmatrix} \bar{w} \\ \bar{c} \end{pmatrix} = \bar{\mathbf{C}} \begin{pmatrix} \bar{w} \\ \bar{c} \end{pmatrix}, \tag{10}$$

or

$$\begin{pmatrix} \bar{w} \\ \bar{c} \end{pmatrix} = \bar{\mathbf{C}}^{-1} \vec{u}^{[j]}, \tag{11}$$

where $\bar{\mathbf{C}} = \bar{\mathbf{H}}$ is the conversion matrix whose inverse can be found using the singular value decomposition (SVD) technique.

For a segment $[j]$ *with interior and boundary points:* Owing to the presence of c_1 and c_2, one can add an additional equation of the form

$$f = \mathbf{K} \begin{pmatrix} \bar{w} \\ \bar{c} \end{pmatrix} \tag{12}$$

to equation system (8). In the case of Neumann boundary conditions, this subsystem can be used to impose a derivative boundary value at $x = x_b$

$$f = \frac{\partial u(x_b)}{\partial x}, \tag{13}$$

$$\mathbf{K} = \begin{bmatrix} H_{[1]}^{(1)}(x_b) & H_{[1]}^{(2)}(x_b) & \ldots & H_{[1]}^{(n_s)}(x_b) & 1 & 0 \end{bmatrix}. \tag{14}$$

The conversion system can be written as

$$\begin{pmatrix} \bar{u}^{[j]} \\ f \end{pmatrix} = \begin{bmatrix} \bar{\mathbf{H}} \\ \mathbf{K} \end{bmatrix} \begin{pmatrix} \bar{w} \\ \bar{c} \end{pmatrix} = \bar{\mathbf{C}} \begin{pmatrix} \bar{w} \\ \bar{c} \end{pmatrix}, \tag{15}$$

or

$$\begin{pmatrix} \bar{w} \\ \bar{c} \end{pmatrix} = \bar{\mathbf{C}}^{-1} \begin{pmatrix} \bar{u}^{[j]} \\ f \end{pmatrix}. \tag{16}$$

It can be seen that (11) is a special case of (16), where f is simply set to null. By substituting Equation (16) into Equations (5)-(7), the second- and first-order derivatives and the function of the variable $u^{[j]}$ are expressed in terms of nodal variable values as

$$\frac{\partial^2 u^{[j]}(x)}{\partial x^2} = \left(H_{[2]}^{(1)}(x), H_{[2]}^{(2)}(x), \ldots, H_{[2]}^{(n_s)}(x), 0, 0 \right) \bar{\mathbf{C}}^{-1} \begin{pmatrix} \bar{u}^{[j]} \\ f \end{pmatrix}, \tag{17}$$

$$\frac{\partial u^{[j]}(x)}{\partial x} = \left(H_{[1]}^{(1)}(x), H_{[1]}^{(2)}(x), \ldots, H_{[1]}^{(n_s)}(x), 1, 0 \right) \bar{\mathbf{C}}^{-1} \begin{pmatrix} \bar{u}^{[j]} \\ f \end{pmatrix}, \tag{18}$$

$$u^{[j]}(x) = \left(H_{[0]}^{(1)}(x), H_{[0]}^{(2)}(x), \ldots, H_{[0]}^{(n_s)}(x), x, 1 \right) \bar{\mathbf{C}}^{-1} \begin{pmatrix} \bar{u}^{[j]} \\ f \end{pmatrix}, \tag{19}$$

or

$$\frac{\partial^2 u^{[j]}(x)}{\partial x^2} = \bar{d}_{2x}^T \bar{u}^{[j]} + k_{2x}(x), \tag{20}$$

$$\frac{\partial u^{[j]}(x)}{\partial x} = \bar{d}_{1x}^T \bar{u}^{[j]} + k_{1x}(x), \tag{21}$$

$$u^{[j]}(x) = \bar{d}_{0x}^T \bar{u}^{[j]} + k_{0x}(x), \tag{22}$$

where k_{0x}, k_{1x} and k_{2x} are scalars whose values depend on x and the boundary value f; and d_{0x}, d_{1x} and d_{2x} known vectors of length n_s.

By application of Equations (20) and (21) to n_s nodes on the segment $[j]$, the second- and first-order derivatives of $u^{[j]}$ at node x_i are determined as

$$\frac{\partial^2 u^{[j]}(x_i)}{\partial x^2} = \bar{\mathbf{D}}_{2x(idk,:)}\bar{u}^{[j]} + \bar{k}_{2x(idk)}, \tag{23}$$

$$\frac{\partial u^{[j]}(x_i)}{\partial x} = \bar{\mathbf{D}}_{1x(idk,:)}\bar{u}^{[j]} + \bar{k}_{1x(idk)}, \tag{24}$$

$$u^{[j]}(x_i) = \bar{\mathbf{D}}_{0x(idk,:)}\bar{u}^{[j]} + \bar{k}_{0x(idk)} = \bar{\mathbf{I}}_{(idk,:)}\bar{u}^{[j]}, \tag{25}$$

where $\bar{\mathbf{D}}_{1x}$ and $\bar{\mathbf{D}}_{2x}$ are known matrices of dimension $n_s \times n_s$; $\bar{k}_{1x}$ and $\bar{k}_{2x}$ known vectors of length n_s; and idk the index number indicating the location of node x_i in the local network $[j]$. It is noted that $\bar{\mathbf{D}}_{0x} = \bar{\mathbf{I}}$, where $\bar{\mathbf{I}}$ is an identity matrix of dimension $n_s \times n_s$ and $\bar{k}_{0x} = \bar{0}$. Therefore, the 1D-IRBFN shape function possesses the Kronecker-δ function properties.

3.2 Incorporation of MLS and 1D-IRBFN into the partition of unity framework

By substituting Equations (23)-(25) into Equations (1)-(4), the function $u(x_i)$ and its derivatives are expressed as

$$u(x_i) = \sum_{j=1}^{n} \bar{m}_{0x}^{[j]}\bar{u}^{[j]}, \tag{26}$$

$$\frac{\partial u(x_i)}{\partial x} = \sum_{j=1}^{n} \left(\bar{m}_{1x}^{[j]}\bar{u}^{[j]} + k_{1x}^{[j]}\right), \tag{27}$$

$$\frac{\partial^2 u(x_i)}{\partial x^2} = \sum_{j=1}^{n} \left(\bar{m}_{2x}^{[j]}\bar{u}^{[j]} + k_{2x}^{[j]}\right), \tag{28}$$

where

$$\bar{m}_{0x}^{[j]} = \bar{\phi}_j(x_i)\bar{\mathbf{I}}_{(idk,:)}, \tag{29}$$

$$\bar{m}_{1x}^{[j]} = \frac{\partial \bar{\phi}_j(x_i)}{\partial x}\bar{\mathbf{I}}_{(idk,:)} + \bar{\phi}_j(x_i)\bar{\mathbf{D}}_{1x(idk,:)}, \tag{30}$$

$$\bar{m}_{2x}^{[j]} = \frac{\partial^2 \bar{\phi}_j(x_i)}{\partial x^2}\bar{\mathbf{I}}_{(idk,:)} + 2\frac{\partial \bar{\phi}_j(x_i)}{\partial x}\bar{\mathbf{D}}_{1x(idk,:)} + \bar{\phi}_j(x_i)\bar{\mathbf{D}}_{2x(idk,:)}, \tag{31}$$

$$k_{1x}^{[j]} = \bar{\phi}_j(x_i)\bar{k}_{1x(idk)}, \tag{32}$$

$$k_{2x}^{[j]} = 2\frac{\partial \bar{\phi}_j(x_i)}{\partial x}\bar{k}_{1x(idk)} + \bar{\phi}_j(x_i)\bar{k}_{2x(idk)}. \tag{33}$$

From Equations (2), (26) and (29), one can see that the LMLS-1D-IRBFN shape function possesses the Kronecker-δ function properties. Equations (27) and (28) can be expressed as

$$\frac{\partial u(x_i)}{\partial x} = \bar{m}_{1x}^{[i]} \bar{u}^{[i]} + k_{1x}^{[i]}, \tag{34}$$

$$\frac{\partial^2 u(x_i)}{\partial x^2} = \bar{m}_{2x}^{[i]} \bar{u}^{[i]} + k_{2x}^{[i]}, \tag{35}$$

where $\bar{u}^{[i]} = \left(u^{(1)}, u^{(2)}, ..., u^{(n_r)}\right)^T$; n_r is the number of nodes in the network $[i]$; $k_{1x}^{[i]}$ and $k_{2x}^{[i]}$ known scalars; and $\bar{m}_{1x}^{[i]}$ and $\bar{m}_{2x}^{[i]}$ known vectors of length n_r, defined by

$$\bar{m}_{1x(id\,j)}^{[i]} = \bar{m}_{1x(id\,j)}^{[i]} + \bar{m}_{1x}^{[j]}, \qquad j = 1, 2, ..., n \tag{36}$$

$$\bar{m}_{2x(id\,j)}^{[i]} = \bar{m}_{2x(id\,j)}^{[i]} + \bar{m}_{2x}^{[j]}, \qquad j = 1, 2, ..., n \tag{37}$$

in which $id\,j$ is the index vector mapping the location of nodes of the local network $[j]$ to that in the LMLS-1D-IRBF network $[i]$.

The values of first- and second-order derivatives of u with respect to x at the nodal points on the grid line $[l]$ are given by

$$\frac{\partial \hat{u}}{\partial x} = \hat{\mathbf{M}}_{1x}^{[l]} \hat{u}^{[l]} + \hat{k}_{1x}^{[l]}, \tag{38}$$

$$\frac{\partial^2 \hat{u}}{\partial x^2} = \hat{\mathbf{M}}_{2x}^{[l]} \hat{u}^{[l]} + \hat{k}_{2x}^{[l]}, \tag{39}$$

where

$$\hat{u} = \left(u^{(1)}, u^{(2)}, ..., u^{(n_l)}\right)^T, \tag{40}$$

$$\hat{\mathbf{M}}_{1x(i,idi)}^{[l]} = \bar{m}_{1x}^{[i]}, \tag{41}$$

$$\hat{\mathbf{M}}_{2x(i,idi)}^{[l]} = \bar{m}_{2x}^{[i]}, \tag{42}$$

$$\hat{k}_{1x(i)}^{[l]} = k_{1x}^{[i]}, \tag{43}$$

$$\hat{k}_{2x(i)}^{[l]} = k_{2x}^{[i]}, \tag{44}$$

in which n_l is the number of nodes on the grid line $[l]$, and idi the index vector mapping the location of nodes of the local network $[i]$ to that in the grid line $[l]$.

The values of first- and second-order derivatives of u with respect to x at the nodal

points over the problem domain are given by

$$\frac{\partial \tilde{u}}{\partial x} = \tilde{\mathbf{M}}_{1x}\tilde{u} + \tilde{k}_{1x}, \tag{45}$$

$$\frac{\partial^2 \tilde{u}}{\partial x^2} = \tilde{\mathbf{M}}_{2x}\tilde{u} + \tilde{k}_{2x}, \tag{46}$$

where

$$\tilde{u} = \left(u^{(1)}, u^{(2)}, ..., u^{(N_{ip})}\right)^T, \tag{47}$$

$$\frac{\partial \tilde{u}}{\partial x} = \left(\frac{\partial u^{(1)}}{\partial x}, \frac{\partial u^{(2)}}{\partial x}, ..., \frac{\partial u^{(N_{ip})}}{\partial x}\right)^T, \tag{48}$$

$$\frac{\partial^2 \tilde{u}}{\partial x^2} = \left(\frac{\partial^2 u^{(1)}}{\partial x^2}, \frac{\partial^2 u^{(2)}}{\partial x^2}, ..., \frac{\partial^2 u^{(N_{ip})}}{\partial x^2}\right)^T, \tag{49}$$

and $\tilde{\mathbf{M}}_{1x}$ and $\tilde{\mathbf{M}}_{2x}$ are known matrices of dimension $N_{ip} \times N_{ip}$; $\tilde{k}_{1x}$ and $\tilde{k}_{2x}$ known vectors of length N_{ip}; and N_{ip} the total number of interior nodal points. The matrices $\tilde{\mathbf{M}}_{1x}$ and $\tilde{\mathbf{M}}_{2x}$ and the vectors $\tilde{k}_{1x}$ and $\tilde{k}_{2x}$ are formed as follows.

$$\tilde{\mathbf{M}}_{1x(idl,idl)} = \hat{\mathbf{M}}^{[l]}_{1x}, \tag{50}$$

$$\tilde{\mathbf{M}}_{2x(idl,idl)} = \hat{\mathbf{M}}^{[l]}_{2x}, \tag{51}$$

$$\tilde{k}_{1x(idl)} = \hat{k}^{[l]}_{1x}, \tag{52}$$

$$\tilde{k}_{2x(idl)} = \hat{k}^{[l]}_{2x}, \tag{53}$$

in which *idl* is the index vector mapping the location of nodes on the grid line $[l]$ to that in the whole grid.

Similarly, the values of the second- and first-order derivatives of u with respect to y at the nodal points over the problem domain are given by

$$\frac{\partial \tilde{u}}{\partial y} = \tilde{\mathbf{M}}_{1y}\tilde{u} + \tilde{k}_{1y}, \tag{54}$$

$$\frac{\partial^2 \tilde{u}}{\partial y^2} = \tilde{\mathbf{M}}_{2y}\tilde{u} + \tilde{k}_{2y}. \tag{55}$$

4 Governing equations for natural convection flows

Fluid properties are assumed to be constant except that the density changes with temperature, which is represented by using the Boussinesq approximation. The

dimensionless governing equations, expressed in terms of stream function ψ, vorticity ω and temperature T, are written as

$$\frac{\partial^2\psi}{\partial x^2}+\frac{\partial^2\psi}{\partial y^2}=-\omega, \tag{56}$$

$$\frac{\partial^2\omega}{\partial x^2}+\frac{\partial^2\omega}{\partial y^2}-\frac{1}{\mathrm{Pr}}\frac{\partial\omega}{\partial t}=-Ra\frac{\partial T}{\partial x}+\frac{1}{\mathrm{Pr}}\left(\frac{\partial\psi}{\partial y}\frac{\partial\omega}{\partial x}-\frac{\partial\psi}{\partial x}\frac{\partial\omega}{\partial y}\right), \tag{57}$$

$$\frac{\partial^2 T}{\partial x^2}+\frac{\partial^2 T}{\partial y^2}-\frac{\partial T}{\partial t}=\frac{\partial\psi}{\partial y}\frac{\partial T}{\partial x}-\frac{\partial\psi}{\partial x}\frac{\partial T}{\partial y}, \tag{58}$$

where Pr is the Prandtl number defined as $Pr=\mu C_p/k$, Ra the Rayleigh number defined as $Ra=\left(C_p\rho_0 g\beta_0 L^3\Delta T\right)/(k\nu)$, μ the viscosity, C_p the specific heat at constant pressure, k thermal conductivity, ρ_0 the reference density, g the gravitational acceleration, β_0 the thermal expansion coefficient, L the side length of the square outer cylinder, ΔT the temperature difference between inner and outer cylinders, ν the kinematic viscosity, t the time, and $(x,y)^T$ the position vector. The x and y components of the velocity vector can be defined in terms of the stream function as

$$u=\frac{\partial\psi}{\partial y}, \tag{59}$$

$$v=-\frac{\partial\psi}{\partial x}. \tag{60}$$

The computational boundary conditions for vorticity can be computed as

$$\omega_w=-\left(\frac{\partial^2\psi_w}{\partial x^2}+\frac{\partial^2\psi_w}{\partial y^2}\right) \tag{61}$$

where the subscript w is used to denote quantities on the boundary. For curved boundaries, a formula reported in [Le-Cao, Mai-Duy, and Tran-Cong (2009)] is employed here to derive the vorticity boundary conditions at boundary points on x- and y-grid lines as follows.

$$\omega_w^{(x)}=-\left[1+\left(\frac{t_x}{t_y}\right)^2\right]\frac{\partial^2\psi_w}{\partial x^2}-q_y, \tag{62}$$

$$\omega_w^{(y)}=-\left[1+\left(\frac{t_y}{t_x}\right)^2\right]\frac{\partial^2\psi_w}{\partial y^2}-q_x, \tag{63}$$

where q_x and q_y are known quantities defined by

$$q_x = -\frac{t_y}{t_x^2}\frac{\partial^2 \psi_w}{\partial y \partial s} + \frac{1}{t_x}\frac{\partial^2 \psi_w}{\partial x \partial s}, \tag{64}$$

$$q_y = -\frac{t_x}{t_y^2}\frac{\partial^2 \psi_w}{\partial x \partial s} + \frac{1}{t_y}\frac{\partial^2 \psi_w}{\partial y \partial s}, \tag{65}$$

in which $t_x = \partial x/\partial s, t_y = \partial y/\partial s$ and s is the direction tangential to the curved surface.

Boundary conditions for stream function and temperature are specified in the following examples.

5 Numerical results and discussion

The present method is applied to obtain the solution of two-dimensional Poisson equation in a square domain with a circular hole, and the natural convection in concentric and eccentric annuli. The problem domains are discretised using Cartesian grids. By using the LMLS-1D-IRBFN method to discretise the left hand side (LHS) of governing equations and the LU decomposition technique to solve the resultant sparse system of simultaneous equations, the computational cost and data storage requirements are reduced. In the analyses of natural convection flows, the diffusion terms are discretised using the LMLS-1D-IRBFN method, whereas the nonlinear convection terms are explicitly calculated using the 1D-IRBFN method. As shown in the previous work [Ngo-Cong, Mai-Duy, Karunasena, and Tran-Cong (2012)], this approach yields more accurate solutions than the one using the LMLS-1D-IRBFN to discretise both diffusion and convection terms. In the following Examples 2-4, computational boundary conditions for vorticity are determined by Equations (61)-(65).

5.1 Example 1: Two-dimensional Poisson equation in a square domain with a circular hole

The present method is first verified through the solution of the following 2D Poisson equation

$$\frac{\partial^2 u}{\partial x^2} + \frac{\partial^2 u}{\partial y^2} = 0, \tag{66}$$

defined on a square domain with a square hole as shown in Fig. 2 and subject to Dirichlet boundary conditions. The problem has the following exact solution

$$u_E = (1/\sinh(\pi))\sin(\pi x)\sinh(\pi y), \tag{67}$$

from which the boundary values of u can be derived.

It is noted that the accuracy of RBF-based solution depends on the RBF width, small or large values of the RBF width make the response of neuron too peaked or flat, respectively [Haykin (1999)]. Fig. 3 presents the β-adaptivity study of relative error norm (Ne) and condition number ($cond$) in a range of $4 \leq \beta \leq 10$ by using the LMLS-1D-IRBFN method. It appears that the accuracy increases with increasing value of β for coarse grids. However, the solution becomes unstable at large values of β for dense grids. Therefore, proper values of β are required to obtain good numerical solutions. The condition numbers of the system matrix remains unchanged for different values of β and are slightly different from those of the 1D-IRBFN method.

Tab. 1 describes the grid convergence study of relative error norms (Ne), condition number ($cond$) and percentage of nonzero elements of the system matrix (ε) of the present method with $\beta = 6$ in comparison with those of 1D-IRBFN method. Both methods yield highly accurate results and converge well with increasing node density. It is observed that the convergence order of LMLS-1D-IRBFN (error norm of $O(h^{1.99})$) is smaller than that of 1D-IRBFN (error norm of $O(h^{3.10})$), however, the accuracy of former is better than that of the latter at a given grid size. In addition, the present method is more efficient than the 1D-IRBFN method in terms of memory requirements (e.g., 12.6 times for a grid of 105×105).

5.2 Example 2: Concentric annulus between two circular cylinders

The present method is applied to the solution of natural convection in a concentric annulus between two circular cylinders. The problem geometry and boundary conditions are described in Fig. 4. The parameter values used here are: $Pr = 0.7, L = 1.0$ and $L/D_i = 0.8$, where L is the annulus width, and D_i the inner cylinder diameter. The average equivalent conductivity is given by

$$\overline{k}_{eq} = \frac{-\ln(D_o/D_i)}{2\pi} \oint \frac{\partial T}{\partial n} ds, \tag{68}$$

where D_o is the diameters of the outer cylinder; and n the direction normal to the cylinder surfaces.

Tab. 2 shows the grid convergence study of average equivalent conductivity on the outer and inner cylinders for Rayleigh numbers from 10^2 to 7×10^4. Three levels of grid density including $41 \times 41, 51 \times 51$ and 61×61 are considered. The present numerical results are compared with the 1D-IRBFN, FDM and DQM results obtained by Le-Cao, Mai-Duy, and Tran-Cong (2009); Kuehn and Goldstein (1976); and Shu (1999), respectively. It can be seen that the present results converge to those reference values with increasing grid density.

Figs. 5 and 6 show the influence of Rayleigh number on the equivalent conductivities on the inner and outer the cylinders, respectively. The figures indicate that heat is being convected from the lower portion of the inner cylinder to the top of the outer cylinder.

Figs. 7 and 8 present the contours of temperature and stream function of the flow in the annulus for Rayleigh numbers from 10^2 to 7×10^4. Those contours are symmetric with respect to the vertical center line. At low Rayleigh numbers (say $< 10^2$), the flow appears almost symmetric about the horizontal center line since convection is quite small. As the Rayleigh number increases, the center of rotation moves upwards and the temperature distribution become distorted, resulting in an increase in overall heat transfer. The highest local heat flux occurs at the stagnation point while the smallest local heat flux occurs at the separation point. For the inner cylinder, the stagnation point is at the bottom while the separation point is at the top. For the outer cylinder, the stagnation point is at the top while the separation point is at the bottom.

5.3 Example 3: Concentric annulus between a square outer cylinder and a circular inner cylinder

This example is concerned with the natural convection in a concentric annulus between a square outer cylinder and a circular inner cylinder. The problem geometry and boundary conditions are depicted in Fig. 9. The parameter values used here are: $Pr = 0.71$ and $L/2R = 2.5$, where L is the side length of the outer square, and R the radius of the inner cylinder. The average Nusselt number is defined by

$$Nu = -\frac{1}{k} \oint \frac{\partial T}{\partial n} ds, \tag{69}$$

where k is the thermal conductivity.

Tab. 3 presents the grid convergence study of the average Nusselt number on the inner and the outer cylinders for different Raleigh numbers. Moukalled and Acharya (1996) studied this problem by solving the governing elliptic conservation equations in a boundary-fitted coordinate system using a control volume-based procedure. The governing equations were solved for only one-half of the physical domain since the flow is symmetric about the vertical axis. In the present study, a whole of the physical domain is considered. Therefore, the average Nusselt numbers obtained are divided by 2 for the purposes of comparison. It can be seen that the present results converge to the 1D-IRBFN [Le-Cao, Mai-Duy, and Tran-Cong (2009)] and FDM [Moukalled and Acharya (1996)] results with increasing grid density.

Fig. 10 shows the contours of temperature, stream function and vorticity of the flow

field inside the enclosure for different Rayleigh numbers. The numerical results obtained are symmetric about the vertical center line. The contours of stream function shows that the flow moves up along the inner cylinder wall and the vertical axis to reach the top of the outer cylinder, and then moves down along the outer cylinder wall. There are boundary layers near the bottom of the inner cylinder and near the top of the outer cylinder, while a flow separation occurs near the top of the inner cylinder which forms a thermal plume. Those behaviours agree well with published results in the literature.

5.4 Example 4: Eccentric annulus between a square outer cylinder and a circular inner cylinder

Natural convection heat transfer between a heated circular cylinder placed eccentrically inside a square cylinder is studied. The stream function value on the outer wall is taken to be zero, while the stream function value on the inner wall (ψ_{wall}) is unknown, which can be determined by using a single-valued pressure condition through the following equation.

$$\oint_{\Gamma} \frac{\partial^3 \psi}{\partial y \partial x^2} dx + \oint_{\Gamma} \frac{\partial^3 \psi}{\partial y^3} dx - \oint_{\Gamma} \frac{\partial^3 \psi}{\partial x^3} dy - \oint_{\Gamma} \frac{\partial^3 \psi}{\partial x \partial y^2} dy = 0. \tag{70}$$

where Γ is the inner boundary. The reader is referred to the work of Le-Cao, Mai-Duy, Tran, and Tran-Cong (2011) for further details. The geometry and boundary conditions of the present problem are described in Fig. 11, where φ is the angular position of the center of the inner cylinder, R the radius of the inner cylinder and L the side length of the outer square. The dimensionless eccentricity is defined by $\varepsilon_0 = \varepsilon/(L/2-R)$, where ε is the distance between the centers of the inner and outer cylinders. The simulation is conducted with the parameter values $Pr = 0.71, Ra = 3\times 10^5$ and $L/2R = 2.6$.

The comparison of the maximum stream-function value ψ_{max}, the stream-function values on the inner cylinder ψ_{wall} and the average Nusselt number among the present method and the other methods for different values of ε_0 and φ are shown in Tabs. 4, 5 and 6, respectively. A grid of 108×108 is taken for the cases $\varepsilon_0 = 0.75$ and $\varphi = 0, -90, 90$, while a grid of 82×82 is used for the other cases. The present results are in good agreement with those of the MQ-DQ [Ding, Shu, Yeo, and Lu (2005)] and 1D-IRBFN [Le-Cao, Mai-Duy, Tran, and Tran-Cong (2011)] methods. The differences of ψ_{max} between the present method and the MQ-DQ and the 1D-IRBFN are less than 1.0% and 1.9%, respectively. The differences of Nusselt numbers between the present results and the MQ-DQ results are less than 1.4%. The differences of ψ_{wall} between the present results with the other results are quite

large due to the sensitivity in the determination of stream function value on the inner cylinder wall, which is also mentioned by Ding, Shu, Yeo, and Lu (2005). Figs. 12, 13, 14, 15, and 16 present the contours of temperature, stream function and vorticity of flow field inside the eccentric annuli with different values of ε_0 and φ. These contours agree well with those in [Ding, Shu, Yeo, and Lu (2005); Le-Cao, Mai-Duy, Tran, and Tran-Cong (2011)].

6 Conclusions

The local MLS-1D-IRBFN method is developed and successfully applied to simulate the natural convection flows in multi-connected domains. The governing equations are formulated in terms of stream function, vorticity and temperature. The unknown stream function value on the inner boundary is determined by using the single-valued pressure condition. The diffusion terms are discretised by using the LMLS-1D-IRBFN while the nonlinear terms are calculated explicitly by using the 1D-IRBFN method. Uniform Cartesian grids are employed to represent all the problem domains. The numerical results showed that the LMLS-1D-IRBFN approximation produces a very sparse system matrix which helps save a lot of memory, while offers a high level of accuracy as that of the 1D-IRBFN method. The numerical results obtained for a wide range of Rayleigh numbers and various geometry parameters are in good agreement with the numerical data available in the literature.

Acknowledgement: This research is supported by the University of Southern Queensland, Australia through a USQ Postgraduate Research Scholarship awarded to D. Ngo-Cong.

References

Atluri, S. N.; Zhu, T. (1998): A new Meshless Local Petrov-Galerkin (MLPG) Approach in Computational Mechanics. *Computational Mechanics*, vol. 22, pp. 117–127.

Banerjee, S.; Mukhopadhyay, A.; Sen, S.; Ganguly, R. (2008): Natural convection in a bi-heater configuration of passive electronic cooling. *International Journal of Thermal Sciences*, vol. 47, pp. 1516–1527.

Costa, V. A. F.; Raimundo, A. M. (2010): Steady mixed convection in a differentially heated square enclosure with an active rotating circular cylinder. *Interational Journal of Heat and Mass Transfer*, vol. 53, pp. 1208–1219.

Ding, H.; Shu, C.; Yeo, K. S.; Lu, Z. L. (2005): Simulation of natural convection in eccentric annuli between a square outer cylinder and a circular inner cylinder using local MQ-DQ method. *Numerical Heat Transfer, Part A*, vol. 47, pp. 291–313.

Divo, E.; Kassab, A. J. (2007): An efficient localized radial basis function meshless method for fluid flow and conjugate heat transfer. *ASME Journal of Heat Transfer*, vol. 129, pp. 124–136.

Haykin, S. (1999): *Neural Networks: A Comprehensive Foundation*. Pearson Prentice-Hall, New Jersey.

Jubran, B. A.; Al-Abdali, H.; Al-Hiddabi, S.; Al-Hinai, H.; Zurigat, Y. (2004): Numerical modelling of convective layers in solar ponds. *Solar Energy*, vol. 77, pp. 339–345.

Kansa, E. J. (1990): Multiquadrics - A Scattered Data Approximation Scheme with Applications to Computational Fulid-Dynamics - II: Solutions to parabolic, Hyperbolic and Elliptic Partial Differential Equations. *Computers & Mathematics with Applications*, vol. 19 (8-9), pp. 147–161.

Kim, B. S.; Lee, D. S.; Ha, M. Y.; Yoon, H. S. (2008): A numerical study of natural convection in a square enclosure with a circular cylinder at different vertical locations. *International Journal of Heat and Mass Transfer*, vol. 51, pp. 1888–1906.

Kuehn, T. H.; Goldstein, R. J. (1976): An experimental and theoretical study of naturl convection in the annulus between horizontal concentric cylinders. *The Journal of Fluid Mechanics*, vol. 74 (4), pp. 695–719.

Le, P. B. H.; Rabczuk, T.; Mai-Duy, N.; Tran-Cong, T. (2010): A moving IRBFN-based integration-free meshless method. *CMES: Computer Modeling in Engineering & Sciences*, vol. 61 (1), pp. 63–109.

Le-Cao, K.; Mai-Duy, N.; Tran, C.-D.; Tran-Cong, T. (2011): Numerical study of stream-function formulation governing flows in multiply-connected domains by integrated RBFs and Cartesian grids. *Computers & Fluids*, vol. 44 (1), pp. 32–42.

Le-Cao, K.; Mai-Duy, N.; Tran-Cong, T. (2009): An effective integrated-RBFN Cartesian-grid discretization for the stream function-vorticity-temperature formulation in nonrectangular domains. *Numerical Heat Transfer, Part B*, vol. 55, pp. 480–502.

Lee, C. K.; Liu, X.; Fan, S. C. (2003): Local multiquadric approximation for solving boundary value problems. *Computational Mechanics*, vol. 30, pp. 396–409.

Lewis, E. (1979): Steady flow between a rotating circular cylinder and fixed square cylinder. *The Journal of Fluid Mechanics*, vol. 95 (3), pp. 497–513.

Liu, G. R. (2003): *Meshfree Methods: Moving Beyond the Finite Element Method*. CRC Press, London.

Mai-Duy, N.; Tanner, R. I. (2007): A Collocation Method based on One-Dimensional RBF Interpolation Scheme for Solving PDEs. *International Journal of Numerical Methods for Heat & Fluid Flow*, vol. 17 (2), pp. 165–186.

Mai-Duy, N.; Tran-Cong, T. (2001): Numerical solution of differential equations using multiquadric radial basis function networks. *Neural Networks*, vol. 14, pp. 185–199.

Mai-Duy, N.; Tran-Cong, T. (2001): Numerical Solution of Navier-Stokes Equations using Multiquadric Radial Basis Function Networks. *International Journal for Numerical Methods in Fluids*, vol. 37, pp. 65–86.

Moukalled, F.; Acharya, S. (1996): Natural convection in the annulus between concentric horizontal circular and square cylinders. *Journal of Thermophysics and Heat Transfer*, vol. 10 (3), pp. 524–531.

Ngo-Cong, D.; Mai-Duy, N.; Karunasena, W.; Tran-Cong, T. (2011): Free vibration analysis of laminated composite plates based on FSDT using one-dimensional IRBFN method. *Computers & Structures*, vol. 89, pp. 1–13.

Ngo-Cong, D.; Mai-Duy, N.; Karunasena, W.; Tran-Cong, T. (2012): Local Moving Least Square - One-Dimensional IRBFN Technique for Incompressible Viscous Flows. *International Journal for Numerical Methods in Fluids*, pg. (published online 9/Jan/2012 DOI: 10.1002/fld.3640).

Russell, D.; Wang, Z. J. (2003): A Cartesian grid method for modeling multiple moving objects in 2D incompressible viscous flow. *Journal of Computational Physics*, vol. 191, pp. 177–205.

Šarler, B.; Perko, J. (2004): Radial basis function collocation method solution of natural convection in porous media. *International Journal of Numerical Methods for Heat & Fluid Flow*, vol. 14 (2), pp. 187–212.

Šarler, B.; Vertnik, R. (2006): Meshfree explicit local radial basis function collocation method for diffusion problems. *Computers and Mathematics with Applications*, vol. 51, pp. 1269–1282.

Shu, C. (1999): Appication of differential quadrature method to simulate natural convection in a concentric annulus. *International Journal for Numerical Methods in Fluids*, vol. 30, pp. 977–993.

Shu, C.; Ding, H.; Yeo, K. S. (2003): Local radial basis function-based differential quadrature method and its application to solve two-dimensional incompressible Navier-Stokes equations. *Computer Methods in Applied Mechanics and Engineering*, vol. 192, pp. 941–954.

Shu, C.; Ding, H.; Yeo, K. S. (2005): Computation of Incompressible Navier-Stokes equations by local RBF-based differential quadrature method. *CMES: Computer Modeling in Engineering & Sciences*, vol. 7 (2), pp. 195–205.

Shu, C.; Xue, H.; Zhu, Y. D. (2001): Numerical study of natural convection in an eccentric annulus between a square outer cylinder and a circular inner cylinder using DQ method. *International Journal of Heat and Mass Transfer*, vol. 44, pp. 3321–3333.

Shu, C.; Zhu, Y. D. (2002): Efficient computation of natural convection in a concentric annulus between an outer square cylinder and an inner circular cylinder. *International Journal for Numerical Methods in Fluids*, vol. 38, pp. 429–445.

Tezduyar, T. E.; Glowinski, R.; Liou, J. (1988): Petrov-Galerkin methods on multiply connected domains for the vorticity-stream function formulation of the incompressible Navier-Stokes equations. *International Journal for Numerical Methods in Fluids*, vol. 8, pp. 1269–1290.

Vertnik, R.; Šarler, B. (2006): Meshless local radial basis function collocation method for convective-diffusive solid-liquid phase change problems. *International Journal of Numerical Methods for Heat and Fluid Flow*, vol. 16, pp. 617–640.

Vertnik, R.; Šarler, B. (2009): Solution of incompressible turbulent flow by a mesh-free method. *CMES: Computer Modeling in Engineering & Sciences*, vol. 44 (1), pp. 65–95.

Wang, J. G.; Liu, G. R. (2002): A Point Interpolation Meshless Method based on Radial Basis Function. *International Journal for Numerical Methods in Engineering*, vol. 54, pp. 1623–1648.

Yao, G.; Šarler, B.; Chen, C. S. (2011): A comparison of three explicit local meshless methods using radial basis functions. *Engineering Analysis with Boundary Elements*, vol. 35, pp. 600–609.

Ye, T.; Mittal, R.; Udaykumar, H. S.; Shyy, W. (1999): An accurate Cartesian grid method for viscous incompressible flows with complex immersed boundaries. *Journal of Computational Physics*, vol. 156, pp. 209–240.

Zerroukat, M.; Djidjeli, K.; Charafi, A. (2000): Explicit and implicit meshless methods for linear advection-diffusion-type partial differential equations. *International Journal for Numerical Methods in Engineering*, vol. 48, pp. 19–35.

Table 1: Poisson equation in a square domain with a circular hole subject to Dirichlet boundary conditions: comparison of relative error norm (Ne), condition number ($cond$) and percentage of nonzero elements of the system matrix (ε), using $\beta = 1$ for 1D-IRBFN and $\beta = 6$ for the present method (LMLS-1D-IRBFN).

Grid	Ne		$cond$		$\varepsilon(\%)$	
	1D-IRBFN	Present	1D-IRBFN	Present	1D-IRBFN	Present
25×25	3.38E-05	5.82E-06	3.31E+02	3.32E+02	7.79	2.48
33×33	1.34E-05	3.05E-06	3.56E+02	3.74E+02	5.79	1.43
41×41	6.65E-06	2.00E-06	5.96E+02	6.06E+02	4.55	0.92
49×49	3.87E-06	1.42E-06	9.00E+02	8.97E+02	3.84	0.64
57×57	2.38E-06	1.05E-06	1.66E+03	1.68E+03	3.26	0.47
65×65	1.58E-06	7.97E-07	2.28E+03	2.38E+03	2.88	0.36
73×73	1.09E-06	6.33E-07	2.99E+03	3.07E+03	2.54	0.29
81×81	7.89E-07	5.18E-07	4.06E+03	4.17E+03	2.27	0.23
89×89	5.90E-07	4.19E-07	4.05E+03	4.10E+03	2.09	0.19
97×97	4.48E-07	3.62E-07	4.50E+03	4.54E+03	1.90	0.16
105×105	3.53E-07	3.03E-07	6.02E+03	6.30E+03	1.77	0.14

Table 2: Concentric annulus between two circular cylinders: Grid convergence study of the average equivalent conductivity on the outer and inner cylinders, k_{eqo} and k_{eqi}, respectively, for different Rayleigh numbers.

Ra	10^2	10^3	3×10^3	6×10^3	10^4	5×10^4	7×10^4
Grid				k_{eqi}			
41×41	1.002	1.083	1.397	1.716	1.983	3.107	3.462
51×51	1.001	1.083	1.399	1.719	1.984	3.017	3.288
61×61	1.001	1.083	1.398	1.717	1.982	2.983	3.238
1D-IRBFN[a]	1.000	1.083	1.396	1.709	1.975	2.962	3.207
FDM[b]	1.000	1.081	1.404	1.736	2.010	3.024	3.308
DQM[c]	1.001	1.082	1.397	1.715	1.979	2.958	
				k_{eqo}			
41×41	1.001	1.083	1.399	1.715	1.969	3.264	3.733
51×51	1.001	1.083	1.399	1.718	1.979	2.996	3.394
61×61	1.001	1.083	1.398	1.717	1.981	2.927	3.218
1D-IRBFN[a]	0.999	1.080	1.393	1.712	1.970	2.942	3.246
FDM[b]	1.002	1.084	1.402	1.735	2.005	2.973	3.226
DQM[c]	1.001	1.082	1.397	1.715	1.979	2.958	

[a] [Le-Cao, Mai-Duy, and Tran-Cong (2009)]
[b] [Kuehn and Goldstein (1976)]
[c] [Shu (1999)]

Table 3: Concentric annulus between a square outer cylinder and a circular inner cylinder: Grid convergence study of the average Nusselt number on the inner and outer cylinders, Nu_i and Nu_o, respectively, for different Rayleigh numbers.

Ra	10^4	5×10^4	10^5	5×10^5	10^6
Grid			Nu_i		
43×43	3.23	4.05	4.90	7.58	9.00
53×53	3.23	4.05	4.91	7.56	8.94
63×63	3.23	4.06	4.92	7.55	8.90
1D-IRBFN[a]	3.21	4.04	4.89	7.51	8.85
FDM[b]	3.24		4.86		8.90
DQM[c]	3.33		5.08		9.37
			Nu_o		
43×43	3.22	4.03	4.86	7.31	9.15
53×53	3.22	4.05	4.89	7.38	8.76
63×63	3.23	4.05	4.91	7.43	8.67
1D-IRBFN[a]	3.22	4.04	4.89	7.43	8.70
FDM[b]	3.24		4.86		8.90
DQM[c]	3.33		5.08		9.37

[a] [Le-Cao, Mai-Duy, and Tran-Cong (2009)]
[b] [Moukalled and Acharya (1996)]
[c] [Shu and Zhu (2002)]

Table 4: Eccentric annulus between a square outer cylinder and a circular inner cylinder: Comparison of the maximum stream-function values ψ_{max} for different values of ε_0 and φ.

		ψ_{max}			
φ	ε_0	DQ[a]	MQ-DQ[b]	1D-IRBFN[c]	Present
-90°	0.25	18.67	18.64	18.63	18.64
	0.50	21.43	21.29	21.30	21.34
	0.75	24.07	23.52	23.47	23.68
-45°	0.25	18.84	18.50	18.50	18.53
	0.50	19.75	20.03	20.09	20.11
	0.75	20.65	21.01	21.02	21.06
	0.95	21.68	21.59	21.61	21.63
0°	0.25	17.15	17.00	17.00	17.01
	0.50	18.77	16.97	16.99	16.99
	0.75	16.83	16.84	16.87	16.89
45°	0.25	15.56	15.32	15.31	15.33
	0.50	14.60	14.35	14.23	14.49
	0.75	13.94	13.61	13.52	13.56
	0.95	12.96	12.98	12.91	13.02
90°	0.25	12.55	12.39	12.37	12.41
	0.50	11.32	11.38	11.36	11.41
	0.75	10.26	10.09	10.10	10.11

[a] [Shu, Xue, and Zhu (2001)]
[b] [Ding, Shu, Yeo, and Lu (2005)]
[c] [Le-Cao, Mai-Duy, Tran, and Tran-Cong (2011)]

Table 5: Eccentric annulus between a square outer cylinder and a circular inner cylinder: Comparison of the stream-function values on the inner cylinder ψ_{wall} for different values of ε_0 and φ.

		ψ_{wall}		
φ	ε_0	DQ[a]	MQ-DQ[b]	Present
-90°	0.25	$< 10^{-4}$	$< 10^{-3}$	$< 10^{-3}$
	0.50	$< 10^{-4}$	$< 10^{-3}$	$< 10^{-3}$
	0.75	$< 10^{-4}$	$< 10^{-3}$	$< 10^{-3}$
-45°	0.25	0.11	0.04	0.02
	0.50	0.47	0.46	0.80
	0.75	1.46	1.46	1.09
	0.95	1.80	1.64	1.80
0°	0.25	0.15	0.20	0.27
	0.50	1.64	0.94	0.97
	0.75	1.05	1.35	1.35
45°	0.25	0.12	0.21	0.09
	0.50	0.84	0.69	1.01
	0.75	1.25	1.19	0.87
	0.95	0.93	1.29	1.43
90°	0.25	$< 10^{-4}$	$< 10^{-3}$	$< 10^{-3}$
	0.50	$< 10^{-4}$	$< 10^{-3}$	$< 10^{-3}$
	0.75	$< 10^{-4}$	$< 10^{-3}$	$< 10^{-3}$

[a] [Shu, Xue, and Zhu (2001)]
[b] [Ding, Shu, Yeo, and Lu (2005)]

Table 6: Eccentric annulus between a square outer cylinder and a circular inner cylinder: Comparison of the average Nusselt number Nu for different values of ε_0 and φ.

		Nu		
φ	ε_0	DQ[a]	MQ-DQ[b]	Present
-90°	0.25	6.75	6.74	6.71
	0.50	6.98	6.92	6.88
	0.75	7.95	7.63	7.52
-45°	0.25	6.90	6.64	6.63
	0.50	6.92	6.68	6.62
	0.75	7.06	6.78	6.76
	0.95	7.61	7.29	7.28
0°	0.25	6.73	6.48	6.46
	0.50	6.72	6.42	6.41
	0.75	7.40	7.03	7.03
45°	0.25	6.48	6.29	6.29
	0.50	6.25	6.01	5.99
	0.75	6.23	5.96	5.97
	0.95	6.45	6.36	6.36
90°	0.25	7.05	6.74	6.72
	0.50	6.17	6.15	6.15
	0.75	6.90	6.62	6.62

[a] [Shu, Xue, and Zhu (2001)]

[b] [Ding, Shu, Yeo, and Lu (2005)]

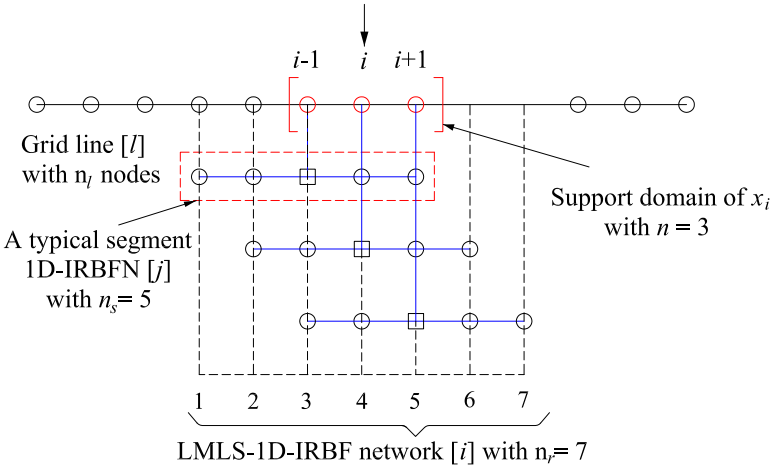

Figure 1: LMLS-1D-IRBFN scheme, □ a typical [j] node.

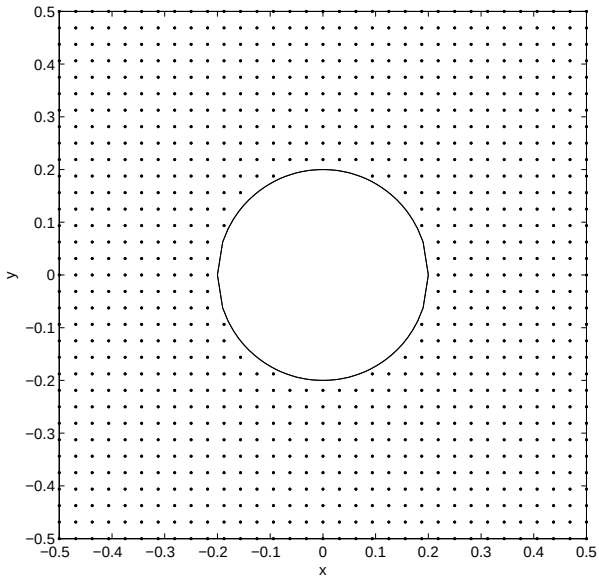

Figure 2: A square domain with a circular hole.

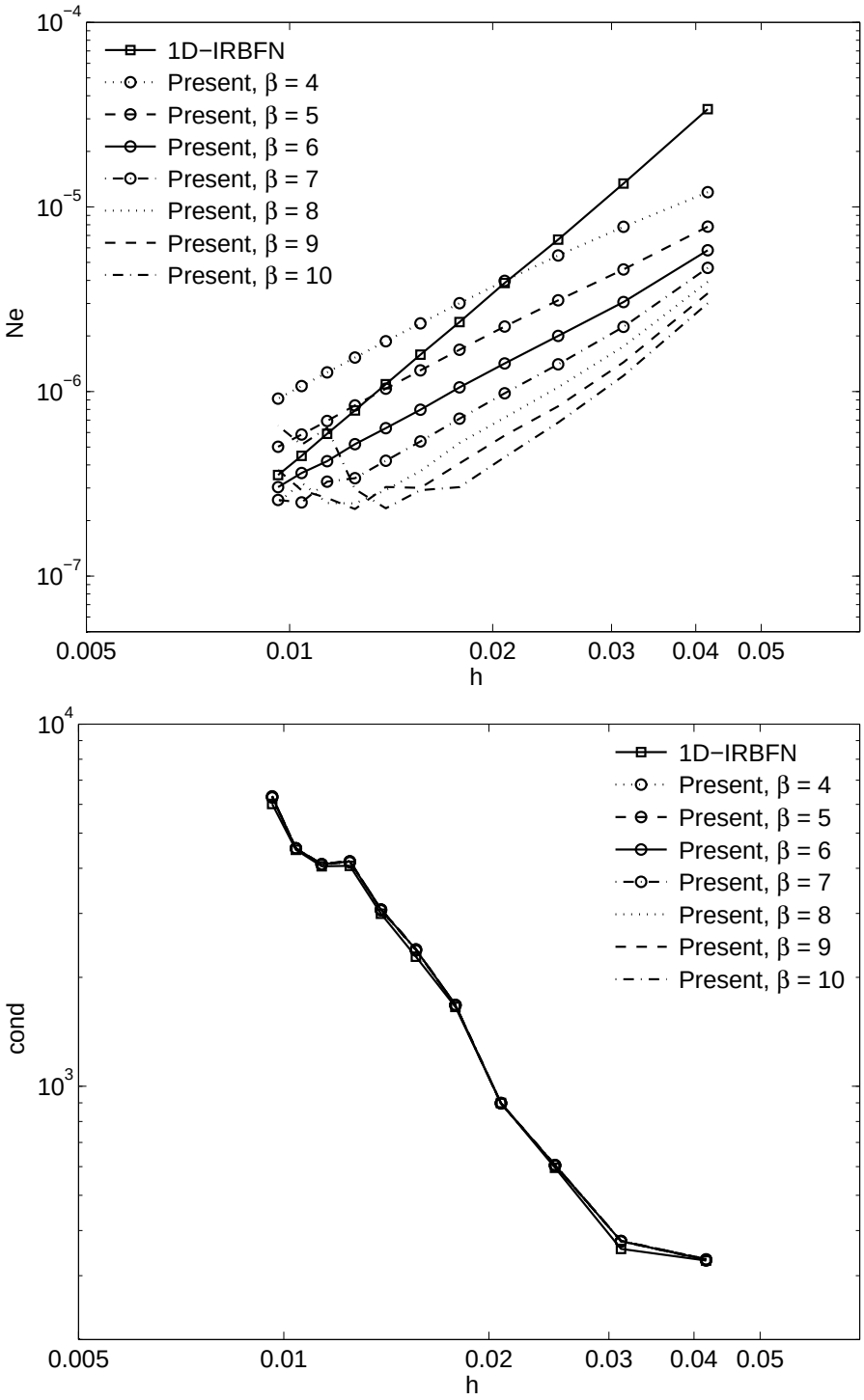

Figure 3: Poisson equation in a square domain with a circular hole subject to Dirichlet boundary conditions: β-adaptivity study for the present method (LMLS-1D-IRBFN).

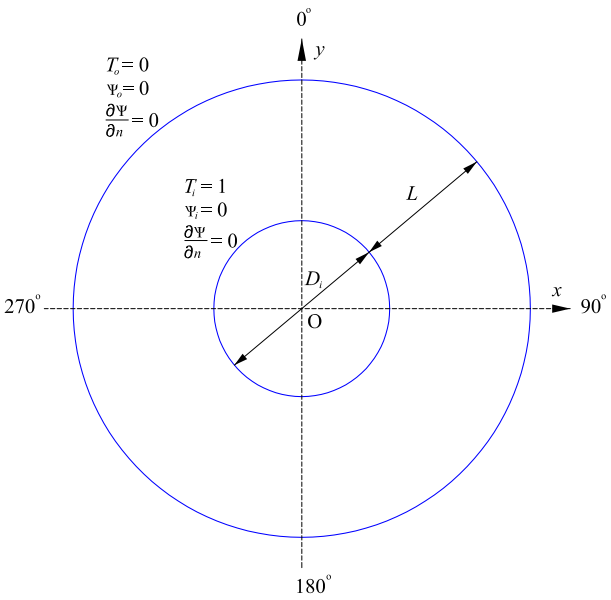

Figure 4: Concentric annulus between two circular cylinders: problem geometry and boundary conditions. Angular positions are measured clockwise from the positive *y*-axis. Note that computational boundary conditions for vorticity are determined by Equations (61)-(65).

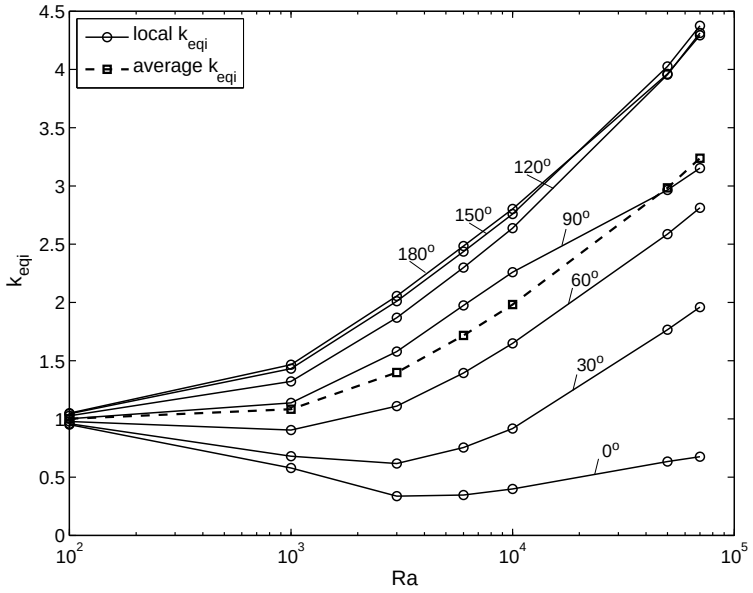

Figure 5: Concentric annulus between two circular cylinders: influence of Rayleigh number on local and average equivalent conductivities on the inner cylinders.

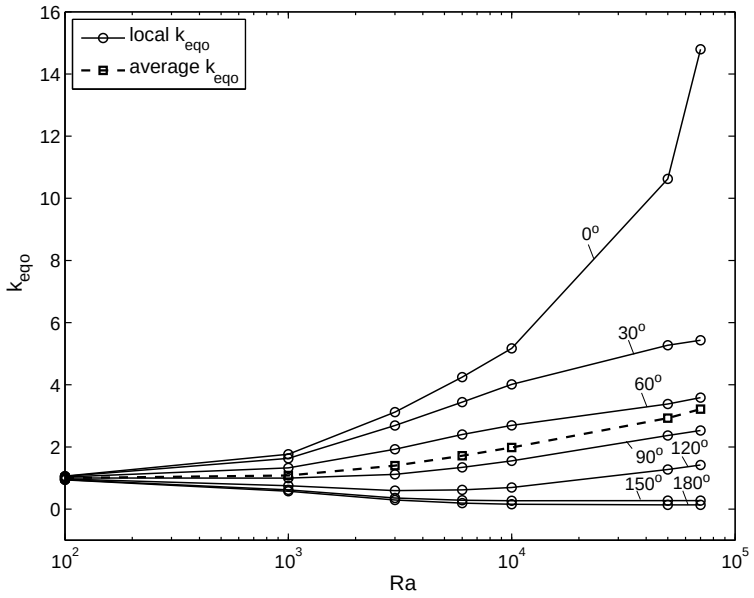

Figure 6: Concentric annulus between two circular cylinders: influence of Rayleigh number on local and average equivalent conductivities on the outer cylinders.

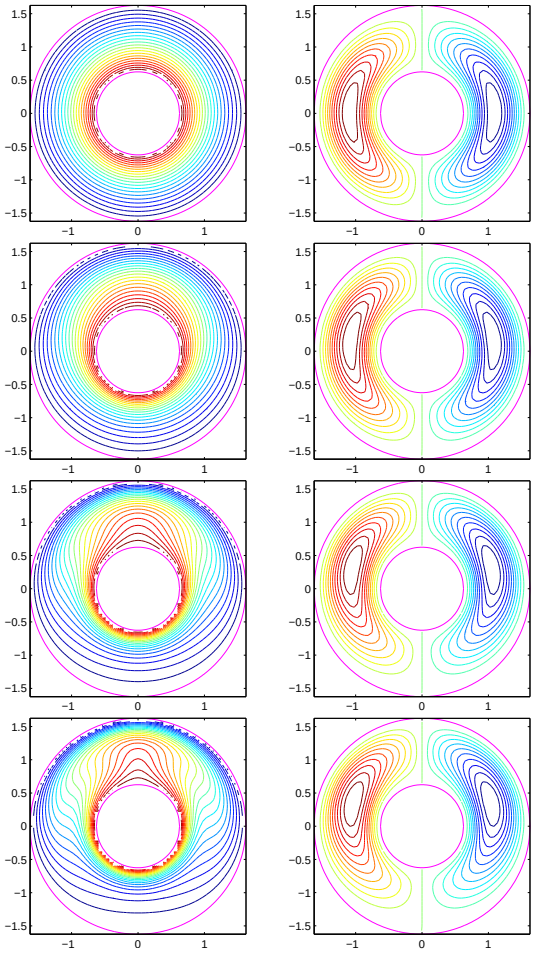

Figure 7: Concentric annulus between two circular cylinders: contours of temperature (left) and stream function (right) for different Rayleigh numbers $Ra = 10^2, 10^3, 3\times10^3$ and 6×10^3, from top to bottom, using a grid of 61×61. Each plot contains 21 contour levels varying linearly from the minimum value to the maximum value.

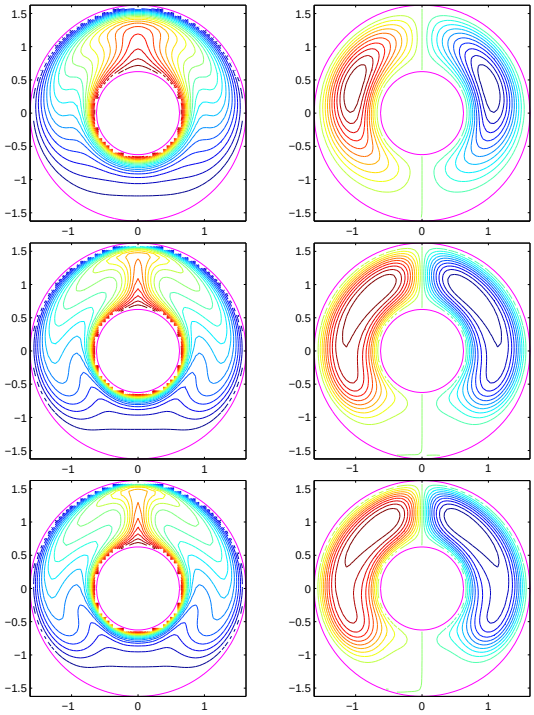

Figure 8: Concentric annulus between two circular cylinders: contours of temperature (left) and stream function (right) for different Rayleigh numbers $Ra = 10^4, 5 \times 10^4$ and 7×10^4, from top to bottom, using a grid of 61×61. Each plot contains 21 contour levels varying linearly from the minimum value to the maximum value.

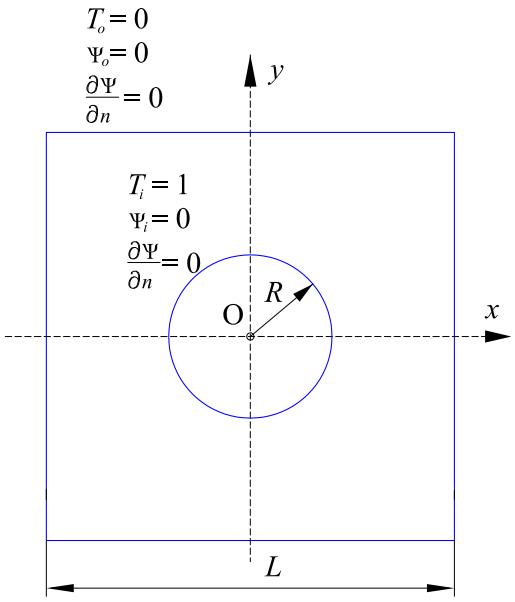

Figure 9: Concentric annulus between a square outer cylinder and a circular inner cylinder: problem geometry and boundary conditions. Note that computational boundary conditions for vorticity are determined by Equations (61)-(65).

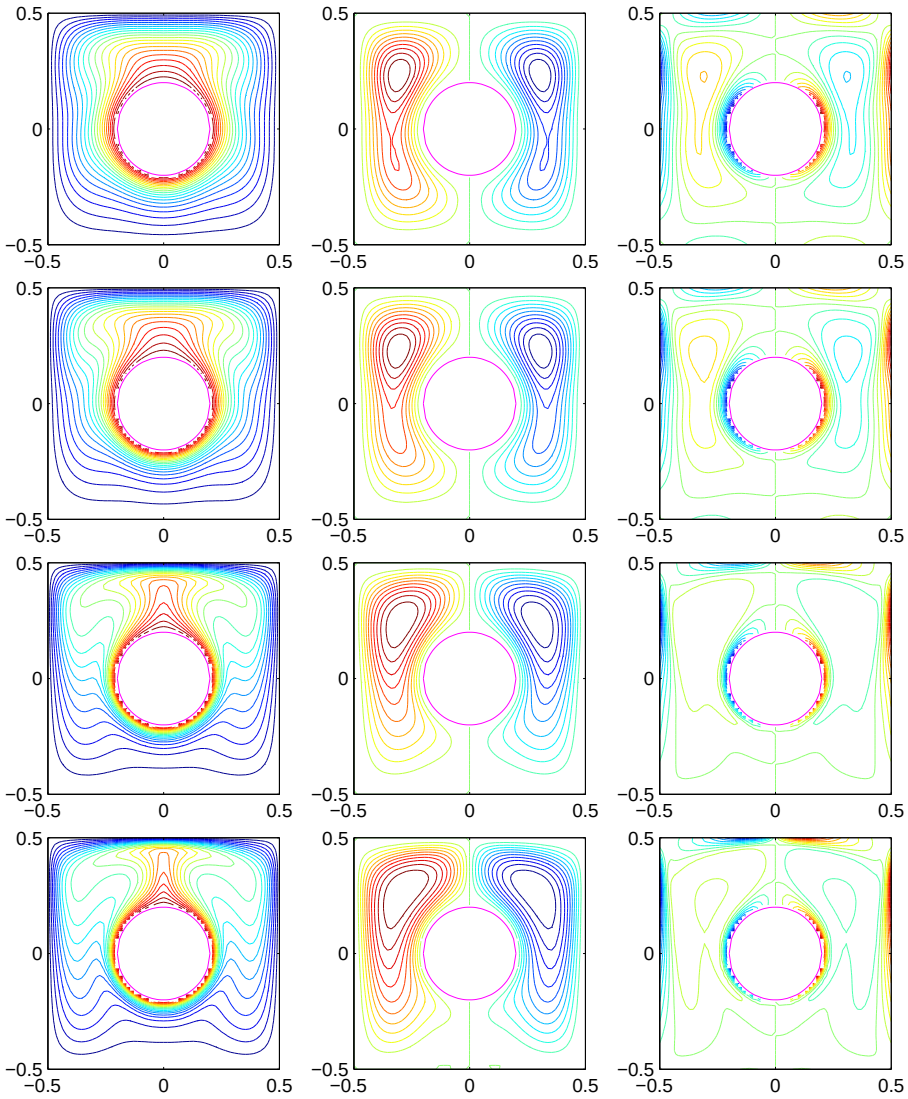

Figure 10: Concentric annulus between a square outer cylinder and a circular inner cylinder: contours of temperature (left), stream function (middle) and vorticity (right) for different Rayleigh numbers $Ra = 5\times10^4, 10^5, 5\times10^5$ and 10^6, from top to bottom, using a grid of 63×63. Each plot contains 21 contour levels varying linearly from the minimum value to the maximum value.

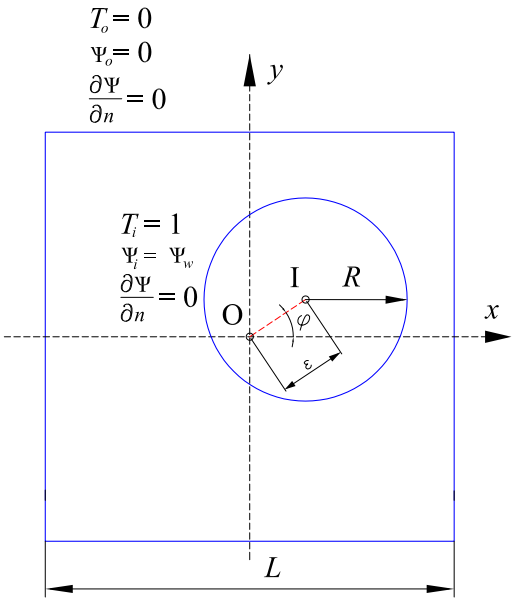

Figure 11: Eccentric annulus between a square outer cylinder and a circular inner cylinder: problem geometry and boundary conditions. The angular position φ of the center of the inner cylinder is measured counterclockwise from the positive x-axis. Note that computational boundary conditions for vorticity are determined by Equations (61)-(65).

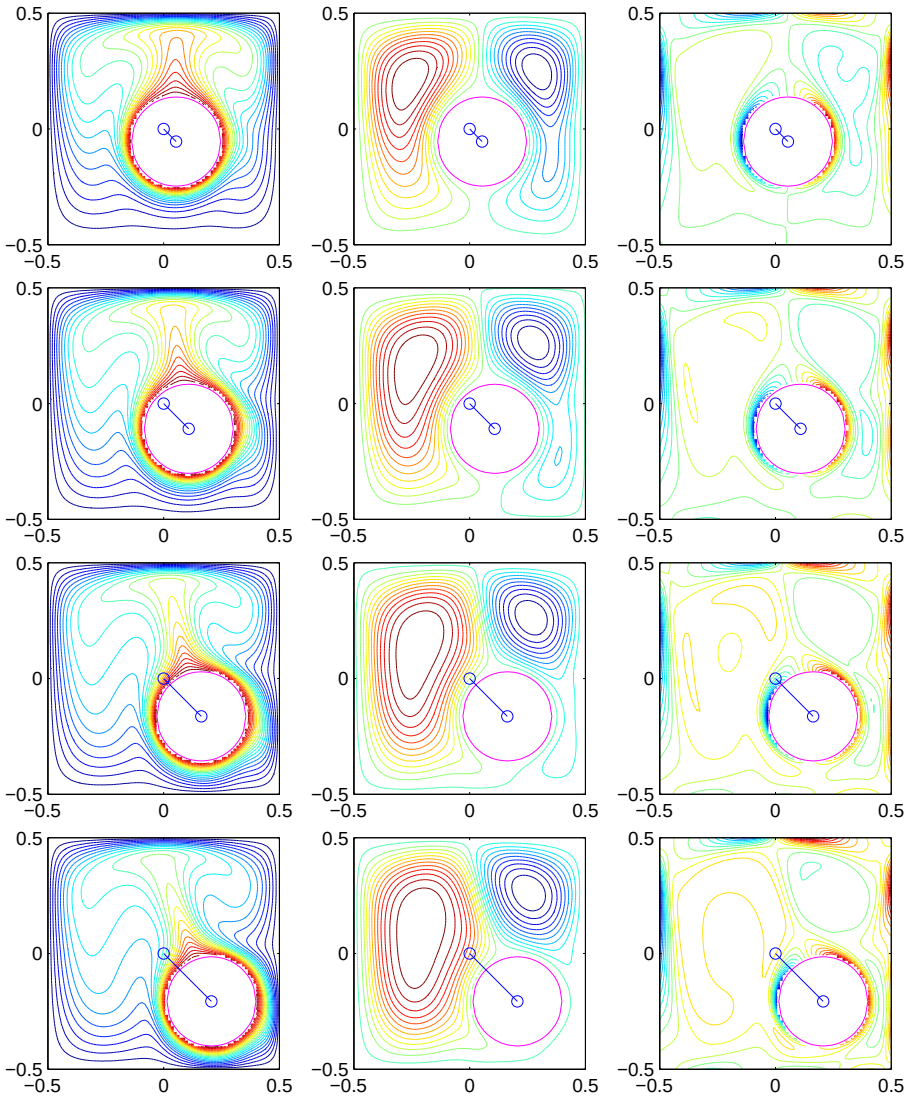

Figure 12: Eccentric annulus between a square outer cylinder and a circular inner cylinder: contours of temperature (left), stream function (middle) and vorticity (right) for the cases of $\varepsilon_0 = 0.25, 0.50, 0.75$ and 0.95, from top to bottom, $Ra = 3 \times 10^5, L/2R = 2.6, \varphi = -45^\circ$, using a grid of 82×82. Each plot contains 21 contour levels varying linearly from the minimum value to the maximum value.

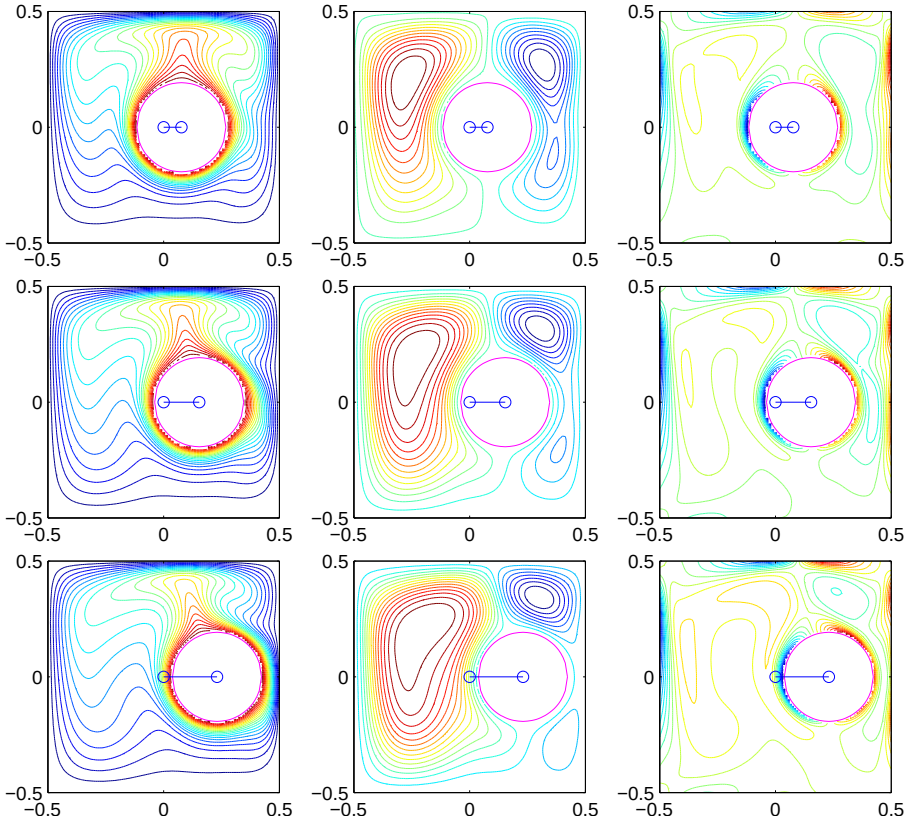

Figure 13: Eccentric annulus between a square outer cylinder and a circular inner cylinder: contours of temperature (left), stream function (middle) and vorticity (right) for the cases of $\varepsilon_0 = 0.25, 0.50$ and 0.75, from top to bottom, $Ra = 3 \times 10^5, L/2R = 2.6, \varphi = 0^\circ$, using a grid of 108×108 for the case $\varepsilon_0 = 0.75$ and a grid of 82×82 for the others. Each plot contains 21 contour levels varying linearly from the minimum value to the maximum value.

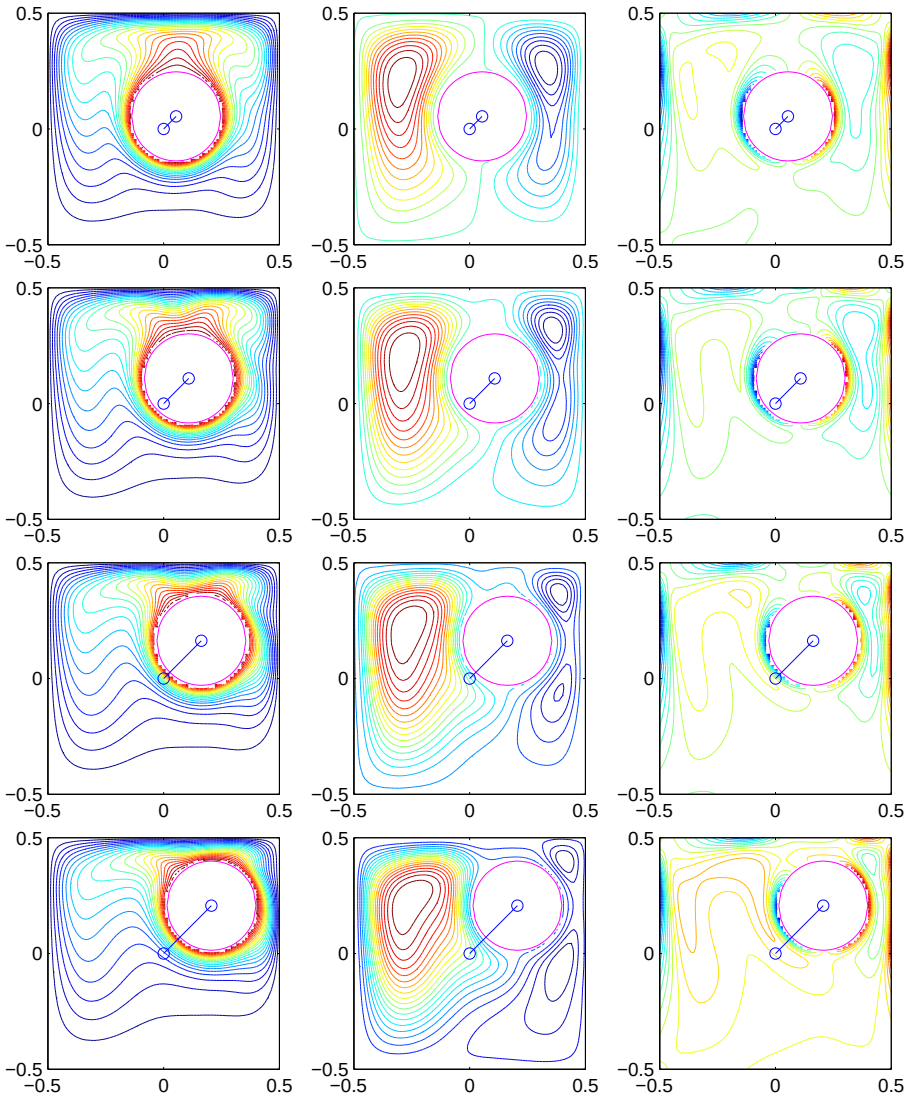

Figure 14: Eccentric annulus between a square outer cylinder and a circular inner cylinder: contours of temperature (left), stream function (middle) and vorticity (right) for the cases of $\varepsilon_0 = 0.25, 0.50, 0.75$ and 0.95, from top to bottom, $Ra = 3 \times 10^5, L/2R = 2.6, \varphi = 45^\circ$, using a grid of 82×82. Each plot contains 21 contour levels varying linearly from the minimum value to the maximum value.

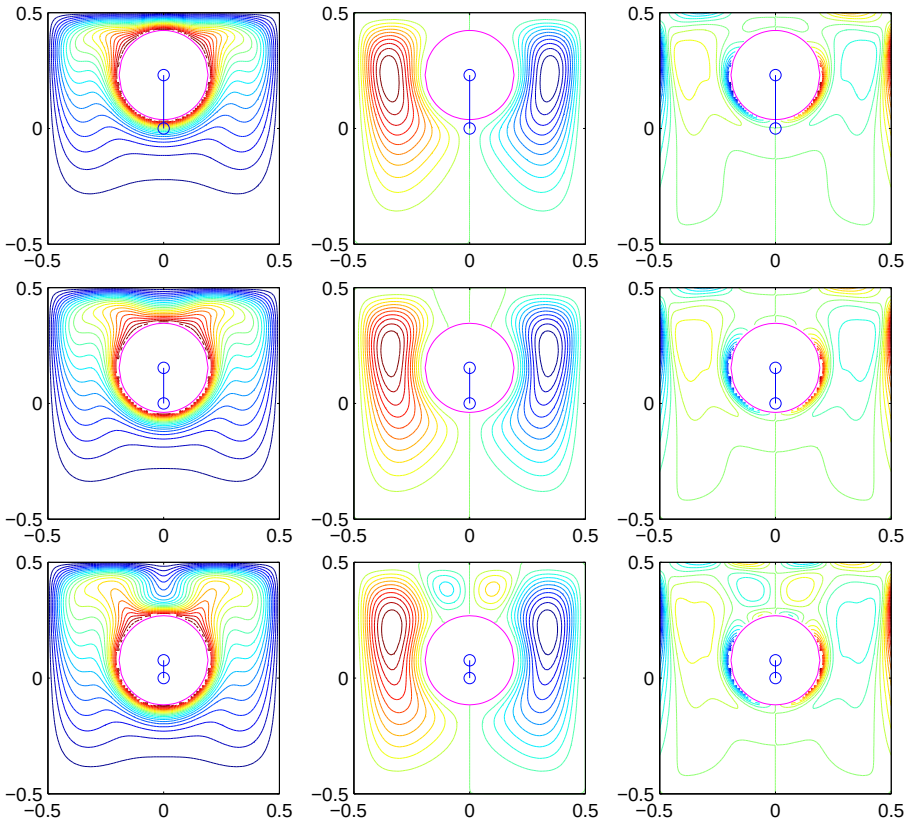

Figure 15: Eccentric annulus between a square outer cylinder and a circular inner cylinder: contours of temperature (left), stream function (middle) and vorticity (right) for the cases of $\varepsilon_0 = 0.75, 0.50$ and 0.25, from top to bottom, $Ra = 3 \times 10^5, L/2R = 2.6, \varphi = 90^\circ$, using a grid of 108×108 for the case $\varepsilon_0 = 0.75$ and a grid of 82×82 for the others. Each plot contains 21 contour levels varying linearly from the minimum value to the maximum value.

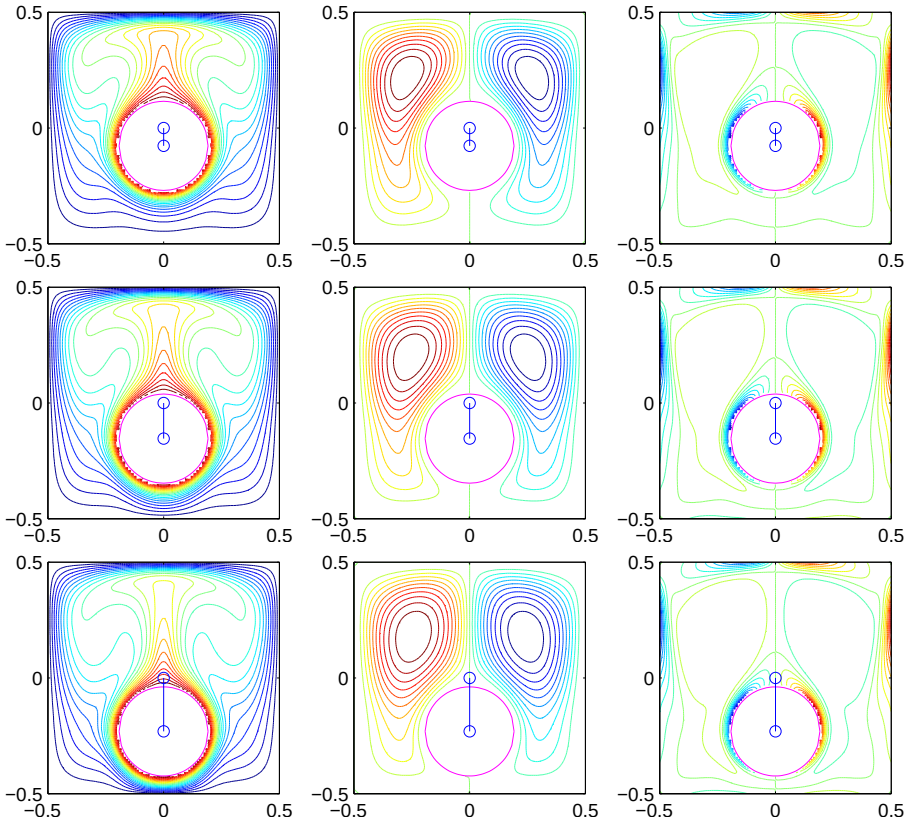

Figure 16: Eccentric annulus between a square outer cylinder and a circular inner cylinder: contours of temperature (left), stream function (middle) and vorticity (right) for the cases of $\varepsilon_0 = 0.25, 0.50$ and 0.75, from top to bottom, $Ra = 3 \times 10^5, L/2R = 2.6, \varphi = -90^\circ$, using a grid of 108×108 for the case $\varepsilon_0 = 0.75$ and a grid of 82×82 for the others. Each plot contains 21 contour levels varying linearly from the minimum value to the maximum value.